Chitosan-modified nickel ferrite nanocomposite for ciprofloxacin adsorption: experimental and density functional theory study

Alaa M. Younis[1]
Qassim University
Mohamed Ali Ben Aissa[1]
Qassim University
Sulaiman Aloraini[1]
Qassim University
Ridha Ben Said[1]
Qassim University
Ali Ben Ahmed[2]
University of Sfax
Abueliz Modwi[1]
Qassim University
Abdullah Alsulami[4]
a.alsulami@qu.edu.sa
Qassim University

Article

Keywords: Ciprofloxacin, Adsorption, Nickel ferrite, Chitosan, Magnetic nanocomposite, Wastewater treatment

Posted Date: August 14th, 2026

DOI: https://doi.org/10.21203/rs.3.rs-10612194/v1

Additional Declarations: No competing interests reported.

Chitosan-modified nickel ferrite nanocomposite for ciprofloxacin adsorption: experimental and density functional theory study

Alaa M. Younis[1], Mohamed Ali Ben Aissa[1], Sulaiman Aloraini[1], Ridha Ben Said[1], Ali Ben Ahmed[2,3], A. Modwi[1] & Abdullah Alsulami[4,*]

[1] Department of Chemistry, College of Science, Qassim University, Buraydah 51452, Saudi Arabia.
[2] University of Sfax, Higher Institute of Biotechnology of Sfax, Department of Biomedical Sciences, Sfax, Tunisia.
[3] University of Sfax, Faculty of Sciences, Laboratory of Applied Physics, Sfax, Tunisia.
[4] Department of Physics, College of Science, Qassim University, Buraydah 51452, Saudi Arabia.
* Correspondence: Abdullah Alsulami, Department of Physics, College of Science, Qassim University, Buraydah 51452, Saudi Arabia. Email: a.alsulami@qu.edu.sa; ORCID: 0000-0001-7355-6921.

Abstract

Antibiotic residues in water motivate the development of accessible adsorbents. A chitosan-modified nickel ferrite nanocomposite ($NiFe_2O_4$@CS) was prepared by *Foeniculum vulgare* seed-extract-assisted synthesis followed by ex situ chitosan incorporation and evaluated for ciprofloxacin (CIP) adsorption. XRD, XPS, SEM–EDS, TEM, and FTIR supported spinel $NiFe_2O_4$ formation and association of chitosan-derived functional groups; Scherrer analysis gave an apparent coherent-domain size of 16.5 nm, and TEM showed ferrite domains of approximately 16–21 nm. Adsorption measurements were conducted at pH 7.0, close to the measured point of zero charge (pH_{pzc} = 6.97). The contact-time experiment yielded $q_{e,exp}$ = 16.82 mg g^{-1}, whereas a separate six-point concentration series gave a maximum directly measured 120-min uptake of approximately 47–48 mg g^{-1}. The Sips equation gave the highest isotherm R^2 (0.989), although its fitted q_m was treated as extrapolated rather than a measured saturation capacity. The pseudo-second-order equation best described kinetics (R^2 = 0.994) without identifying a unique rate-limiting mechanism. Finite-cluster DFT yielded E_{ads} = −0.6069 eV and supported possible hydrogen-bonding, electrostatic and ferrite metal-site contributions. $NiFe_2O_4$@CS therefore adsorbed CIP under single-solute batch conditions, but regeneration, magnetic separability, leaching and real-water performance require experimental validation.

Keywords: Ciprofloxacin; Adsorption; Nickel ferrite; Chitosan; Magnetic nanocomposite; Wastewater treatment

Introduction

Pharmaceutical residues from human and veterinary use are incompletely removed by conventional wastewater treatment and enter surface waters through domestic, hospital, agricultural, aquaculture, and

industrial discharges [1,2]. Antibiotics are particularly concerning because they can disrupt aquatic organisms and microbial communities and may select for antimicrobial-resistance determinants [3–5]. Effective technologies are therefore needed to limit antibiotic release.

Ciprofloxacin (CIP), a widely used fluoroquinolone, is frequently selected as a model pharmaceutical contaminant because of its extensive use, incomplete removal, and pH-dependent speciation [6,7]. Adsorption, photocatalysis, advanced oxidation, membrane separation, and solvent-assisted extraction have been investigated for CIP removal [8,9]. Adsorption is attractive because it is operationally simple, relatively energy-efficient, and compatible with diverse materials, although useful adsorbents must also provide adequate uptake, stability, accessible binding sites, and convenient separation.

Chitosan (CS), a cationic biopolymer obtained by partial deacetylation of chitin, contains amino and hydroxyl groups that interact with contaminants through electrostatic attraction, hydrogen bonding, and complexation [10,11]. However, pH sensitivity, swelling or dissolution under acidic conditions, limited mechanical stability, and difficult recovery restrict its practical use. Combining CS with inorganic particles or carbonaceous materials can improve stability and separation while retaining its functionality [12]. Chitosan-based Fe-Cu composites and graphene oxide beads have been used for CIP adsorption, whereas chitosan-incorporated nickel ferrite has been studied for photocatalytic antibiotic degradation [13–15]. Reviews still identify a need for clearer structure-performance relationships and realistic validation [16,17].

Nickel ferrite ($NiFe_2O_4$) is a spinel oxide with inorganic stability and metal–oxygen surface sites; ferrite composites may also permit magnetic separation when sufficient response is retained [18]. Combining $NiFe_2O_4$ with CS could therefore provide complementary ferrite and polymer binding sites for CIP. Magnetic chitosan adsorbents, biochar-magnetite composites, $NiFe_2O_4$/biochar, and cobalt ferrite/chitosan systems have shown potential for antibiotic removal [19–23]. Nevertheless, direct dark adsorption of CIP by $NiFe_2O_4$/chitosan remains less explored, especially regarding surface-charge context, concentration effects, kinetics, isotherms, and molecular interactions.

This study prepared a chitosan-modified nickel ferrite nanocomposite ($NiFe_2O_4$@CS) for CIP adsorption from water. $NiFe_2O_4$ nanoparticles were produced using a previously developed *Foeniculum vulgare* seed-extract-assisted route [24] and combined with CS. XRD, XPS, SEM–EDS, TEM, and FTIR were used for characterization; batch tests examined initial CIP concentration and contact time, and the point of zero charge was determined. Selected kinetic and isotherm models described the adsorption data, while density functional theory calculations supported interpretation of possible CIP–surface interactions [25]. The study integrates experimental and molecular-level analysis while distinguishing measured uptake from model-derived descriptors.

Methods

Materials

Chitosan powder (molecular weight ≈ 193–400 kDa; degree of deacetylation > 90%), nickel(II) nitrate hexahydrate ($Ni(NO_3)_2 \cdot 6H_2O$, ≥97%), iron(III) nitrate nonahydrate ($Fe(NO_3)_3 \cdot 9H_2O$, ≥98%), ciprofloxacin (CIP, ≥98%), glacial acetic acid (≥99.7%), sodium hydroxide (NaOH, ≥98%), and hydrochloric acid (HCl, 37%) were purchased from Sigma-Aldrich and used as received. Deionized water (18.2 MΩ·cm) was used throughout.

Plant-extract-assisted synthesis of $NiFe_2O_4$ nanoparticles and $NiFe_2O_4$@CS nanocomposite

An aqueous *Foeniculum vulgare* seed extract served as a plant-derived stabilizing/capping medium during $NiFe_2O_4$ synthesis, following a previously reported route with minor adaptation [24].

Preparation of *Foeniculum vulgare* seed extract

Foeniculum vulgare seeds were washed, dried at room temperature, and coarsely ground. Ground seeds (10 g) were stirred in 100 mL deionized water at 80 °C for 1 h. After cooling, the extract was filtered through Whatman No. 42 paper, stored at 4 °C, and used in the subsequent synthesis.

Preparation of $NiFe_2O_4$ nanoparticles

$NiFe_2O_4$ nanoparticles were prepared following Elamin et al. [24]. $Ni(NO_3)_2 \cdot 6H_2O$ (14.5 g, ≈50 mmol) and $Fe(NO_3)_3 \cdot 9H_2O$ (40.4 g, ≈100 mmol) were dissolved in 100 mL deionized water at 60 °C, maintaining a Ni^{2+}:Fe^{3+} molar ratio of 1:2. Seed extract (10 mL) was added slowly under stirring, and the pH was adjusted to ≈10 with 1 M NaOH. The suspension was stirred at 80 °C for 2–3 h until a brown precipitate formed.

The precipitate was centrifuged at 3000 rpm for 5 min, washed repeatedly with deionized water and ethanol to near-neutral pH, and dried at 80 °C for 12 h. The precursor was calcined in air at 600 °C for 4 h (heating rate 5 °C min^{-1}; natural furnace cooling) to obtain crystalline $NiFe_2O_4$ NPs.

Synthesis of $NiFe_2O_4$@CS nanocomposite

$NiFe_2O_4$@CS was prepared by ex situ chitosan deposition. Chitosan (250 mg) was dissolved in 20 mL of 2% (v/v) aqueous acetic acid by sonication for 30 min at room temperature. $NiFe_2O_4$ NPs (250 mg) were separately dispersed in 50 mL deionized water by ultrasonication for 30 min. The chitosan solution was added dropwise to the dispersion under mechanical stirring, followed by probe sonication for 20 min (20 kHz, 700 W) and stirring at 60 °C for 3 h. The composite was precipitated by slowly adding 1 M NaOH and stirring for 1 h, then isolated by centrifugation (4000 rpm, 10 min), washed to near-neutral pH, dried at 60 °C for 12 h, and heated at 120 °C for 2 h.

Characterization techniques

The crystalline phases of chitosan, $NiFe_2O_4$ NPs, and $NiFe_2O_4$@CS were examined by XRD using a Tongda TD-3700 diffractometer with Cu Kα radiation (40 kV, 30 mA). Patterns were recorded over 2θ = 10–80° at 2° min^{-1} with a 0.02° step. Average crystallite size was estimated using the Debye–Scherrer equation, $D = K\lambda/(\beta \cos\theta)$, where K, λ, β, and θ are the shape factor, X-ray wavelength, peak full width at half maximum in radians, and Bragg angle, respectively.

Surface composition and oxidation states were analyzed by XPS using a Thermo ESCALAB 250Xi with monochromated Al Kα radiation; binding energies were calibrated to C 1s at 284.8 eV, and high-resolution Ni 2p, Fe 2p, O 1s, C 1s, and N 1s spectra were recorded. Morphology was examined by SEM (MIRA3-LUM, 15 kV) after applying a 5–10 nm gold coating. SEM–EDS provided elemental composition and Ni, Fe, O, C, and N maps. TEM was performed using a Philips EM 208S at 90 kV after dispersing samples in ethanol and drop-casting them onto carbon-coated copper grids. FTIR spectra before and after CIP adsorption were recorded by the KBr pellet method over 200–4000 cm^{-1} at 4 cm^{-1} resolution.

Adsorption studies

Batch adsorption procedure and investigated parameters

CIP adsorption by $NiFe_2O_4$@CS was evaluated in batch mode. Unless otherwise stated, 100 mL Erlenmeyer flasks containing 50 mL CIP solution were shaken at 150 rpm and 25 ± 1 °C. The flasks were protected from light for dark adsorption tests.

At predetermined intervals, aliquots were centrifuged at 4000 rpm for 10 min, and residual CIP was measured by UV–Vis spectrophotometry at 275 nm. A calibration curve was prepared with fresh external standards within the validated linear range; samples above this range were diluted, and dilution factors were included in the concentration calculations.

The equilibrium adsorption capacity, q_e, and removal percentage, R (%), were calculated using the following equations:

$$q_e = \frac{(C_0 - C_e)V}{m} \quad (1)$$

$$R(\%) = \frac{(C_0 - C_e)}{C_0} \times 100 \quad (2)$$

In the above equations, C_0 and C_e (mg L^{-1}) represent the initial and equilibrium or endpoint CIP concentrations, respectively. V (L) is the solution volume, and m (g) is the mass of dry adsorbent used. All adsorption experiments were performed in triplicate, and plotted values represent the means.

The point of zero charge (pH_{pzc}) of $NiFe_2O_4$@CS was determined by the pH-drift method over an initial-pH range of 2.0–12.0. The measured pH_{pzc} was 6.97. The adsorption experiments reported below were conducted at an initial pH of 7.0, close to pH_{pzc} and within the zwitterionic speciation range of CIP.

Adsorption kinetics

The effect of contact time on CIP adsorption was examined over 0–1440 min under the specified experimental conditions: initial CIP concentration = 20 mg L^{-1}, initial pH = 7.0, temperature = 25 ± 1 °C, agitation speed = 150 rpm, solution volume = 50 mL, and adsorbent mass = 15 mg. The amount of CIP adsorbed at time t was calculated as $q_t = [(C_0 - C_t)V]/m$, where C_t is the residual concentration at time t. The kinetic data were analyzed using pseudo-first-order, pseudo-second-order, and Elovich models to describe the uptake profile and evaluate possible rate-controlling features.

Adsorption isotherm studies

Adsorption isotherm experiments were carried out at nominal initial CIP concentrations of 2.5, 5, 10, 25, 50, and 100 mg L^{-1} under the following conditions: initial pH = 7.0, contact time = 120 min, temperature = 25 ± 1 °C, solution volume = 50 mL, agitation speed = 150 rpm, and adsorbent mass = 20 mg. The residual CIP concentration after adsorption was measured by UV–Vis spectroscopy, and the corresponding adsorption capacity was calculated from the mass-balance equation. The concentration-dependent adsorption data were fitted using Langmuir, Freundlich, Temkin, and Sips isotherm models. The directly observed uptake within the measured concentration range and the fitted model parameters are distinguished in the Results section to avoid treating extrapolated model capacities as experimentally measured maximum capacities. Model fitting was performed using nonlinear least-squares regression.

Computational details

Density functional theory (DFT) and time-dependent density functional theory (TD-DFT) calculations were performed to optimize the selected model structures and estimate electronic descriptors related to CIP interaction with the $NiFe_2O_4$@CS model. The ground-state geometries were optimized using the CAM-B3LYP functional with the LanL2DZ basis set and Grimme D3(BJ) dispersion correction in Gaussian 16 [26–30]. The calculations were conducted using finite molecular/cluster models of stoichiometric $NiFe_2O_4$ unit, a glucosamine-type chitosan fragment, ciprofloxacin in a net-neutral (zwitterionic/near-isoelectric) form, and their corresponding adducts. The CS and CIP models were treated as singlets, whereas the $NiFe_2O_4$-containing models were initialized in a ferrimagnetic arrangement and optimized in an overall triplet state.

Because finite molecular/cluster models were used, the calculated frontier-orbital separations, charge distributions, and work-function-related descriptors were interpreted as model-level indicators rather than experimental bulk band gaps or direct macroscopic thermodynamic quantities. Unless otherwise

stated, solvent, entropy, and concentration effects were not fully included. Frontier molecular orbital energies and global reactivity descriptors were calculated using the following equations [31,32]:

$$\Delta E_{L-H} = E_{LUMO} - E_{HOMO} \quad (3)$$

$$\mu = \frac{(E_{HOMO} + E_{LUMO})}{2} \quad (4)$$

$$\eta = \frac{(E_{LUMO} - E_{HOMO})}{2} \quad (5)$$

$$IP = -E_{HOMO} \quad (6)$$

$$EA = -E_{LUMO} \quad (7)$$

$$\chi = \frac{(EA + IP)}{2} \quad (8)$$

$$S = \frac{1}{\eta} \quad (9)$$

$$\omega = \frac{\mu^2}{2\eta} \quad (10)$$

where ΔEL-H is the HOMO-LUMO energy separation, μ is the electronic chemical potential, η is the chemical hardness, IP is the ionization potential, EA is the electron affinity, χ is the electronegativity, S is the global softness, and ω is the electrophilicity index.

The adsorption energy of CIP on the $NiFe_2O_4$@CS model was calculated using:

$$E_{ads} = E_{NiFe_2O_4@CS-CIP} - (E_{NiFe_2O_4@CS} + E_{CIP}) \quad (11)$$

Within the selected finite-cluster model, a negative E_{ads} indicates an energetically favorable adsorbate–adsorbent interaction. However, this value was interpreted only as a model-level interaction energy and not as direct proof of macroscopic spontaneity or exothermicity under aqueous batch adsorption conditions, because solvent and entropy contributions were not fully represented.

A work-function-related descriptor was also calculated to compare the relative electronic response of $NiFe_2O_4$ toward CS and of $NiFe_2O_4$@CS toward CIP interaction within the selected computational model. This descriptor was calculated as:

$$\Phi = V_{el(+\infty)} - E_{FL} \quad (12)$$

where Vvac represents the electrostatic potential of an electron at a significant distance from the model surface. In this work, Vvac was assumed to be zero; therefore, the work-function-related descriptor is equal to the negative value of the Fermi energy level, EFL. The Fermi energy level was estimated as:

$$E_{\mathrm{FL}} = \frac{E_{\mathrm{HOMO}} + E_{\mathrm{LUMO}}}{2} \quad (13)$$

The calculated descriptors were used only to support the interpretation of possible CIP–$NiFe_2O_4$@CS interactions and were not treated as direct experimental measurements of electronic, sensing, or thermodynamic performance.

Use of AI-assisted tools

ChatGPT (OpenAI) was used for language editing, condensation, organization, and journal-format checking. The authors reviewed and verified all AI-assisted edits and take full responsibility for the manuscript. No AI tool was used to generate, alter, or analyze research data or primary research images.

Results and discussion

Characterization of $NiFe_2O_4$@CS nanocomposite

XRD analysis

Fig. 1 compares the XRD patterns of CS, $NiFe_2O_4$, and $NiFe_2O_4$@CS. CS showed maxima at 2θ = 10.28° and 20.14°, assigned to the (020) and (110) planes, with d-spacings of 0.8598 and 0.4405 nm, respectively; these features are consistent with hydrated, hydrogen-bonded chitosan [33–35]. $NiFe_2O_4$ exhibited the spinel reflections of JCPDS No. 10–0325 at 18.50° (111), 30.38° (220), 35.64° (311), 37.30° (222), 43.54° (400), 54.10° (422), 57.46° (511), 62.08° (440), 75.29° (533), and 79.58° (622), consistent with previous reports [36–38].

In $NiFe_2O_4$@CS, the ferrite reflections were retained, while the CS maxima shifted to 10.84° and 20.30°. Several ferrite peaks weakened and shifted slightly to higher angles; for example, the (311) reflection moved from 35.64° to 35.80°. These changes may reflect interfacial interactions, microstrain, or local disorder, but do not establish lattice contraction without whole-pattern refinement or strain analysis [39]. The (311) FWHM increased from 0.3951° to 0.5062°, and the Scherrer-estimated size decreased from 21.31 nm for $NiFe_2O_4$ to 16.5 nm for $NiFe_2O_4$@CS. Because Scherrer analysis does not separate size, strain, and instrumental broadening, these values are apparent coherent-domain sizes. The coexistence of spinel and chitosan features supports composite formation [40].

XPS analysis

XPS confirmed Ni, Fe, O, C, and N at the $NiFe_2O_4$@CS surface (Fig. 2a). In the high-resolution spectra, Fe $2p_{3/2}$ and Fe $2p_{1/2}$ appeared at 710.8 and 724.6 eV, with satellites at 718.5 and 732.8 eV (Fig. 2c). O

1s components at 529.7, 531.4, and 532.9 eV were assigned to M–O, O=C–N, and C–OH/C–O–C environments; C 1s peaks at 284.7, 286.3, and 288.2 eV to C–C/C–H, C–O/C–N, and O=C–O/O=C–N; and N 1s peaks at 399.5, 400.1, and 401.9 eV to N–H/C–N, O=C–N, and protonated amine (NH_3^+) environments, respectively (Fig. 2d–f) [41].

The combined ferrite-related Ni/Fe/O signals and chitosan-related C/N functionalities provide surface-chemical evidence of composite formation, but do not by themselves prove a continuous or uniformly thick chitosan coating.

SEM–EDS and TEM analysis

SEM images (Fig. 3a–c) showed ferrite nanoparticles distributed within the chitosan matrix. TEM revealed visible $NiFe_2O_4$ domains of about 16–21 nm (Fig. 3d), consistent with the XRD-derived apparent size. The images indicate close ferrite–chitosan contact but do not permit quantitative determination of coating thickness.

EDS of the mapped region detected Fe, Ni, O, C, and N (Supplementary Fig. S1), with approximate contents of 51.2, 25.9, 16.1, 6.0, and 0.8 wt%, respectively [42]. Because EDS is less precise for low-concentration light elements, particularly N, the C/N values are semi-quantitative. Broadly overlapping elemental maps support composite formation without establishing exact homogeneity [43].

Ciprofloxacin adsorption performance

Concentration-dependent CIP adsorption

The 120-min adsorption capacity increased with residual CIP concentration (Fig. 4a), consistent with a stronger concentration gradient and mass-transfer driving force [44]. The directly measured uptake reached about 47–48 mg g^{-1} at the highest plotted concentration. This observed value is distinct from the fitted isotherm-capacity parameters discussed in the adsorption-isotherm analysis.

Point of zero charge and selected adsorption pH

Fig. 4b shows that the pH-drift profile crossed zero at pH_{pzc} = 6.97. CIP is predominantly cationic below pKa1 ≈ 5.9 (–COOH and $>NH_2^+$), zwitterionic between pKa1 and pKa2 ≈ 8.9 ($–COO^-$ and $>NH_2^+$), and anionic above pKa2 ($–COO^-$ and >NH) [20,45]. The $NiFe_2O_4$@CS surface is expected to be more positively charged below pH_{pzc} and more negatively charged above it because of protonation and deprotonation of chitosan $–NH_2$/–OH groups and ferrite surface hydroxyls [46].

At the operating pH of 7.0, which is close to pH_{pzc}, zwitterionic CIP can adopt favorable orientations toward mixed protonated and deprotonated surface sites. Its carboxylate and protonated amine groups may participate in complementary electrostatic interactions, while carbonyl, carboxylate, and amine groups can form hydrogen bonds with chitosan –OH/$–NH_2$ groups [47–49]. This surface-charge context

is consistent with several possible interaction modes, but the proximity of pH 7.0 to pH_{pzc} does not by itself establish an experimentally optimized adsorption pH.

Effect of contact time

Fig. 4c shows rapid initial uptake, reaching about 15–16 mg g^{-1} within 60 min, followed by a slower approach to approximately 16.8–17.2 mg g^{-1} after extended contact. The early stage is consistent with abundant accessible sites and a high concentration gradient, whereas subsequent slowing reflects site occupation and possible diffusion or surface-rearrangement effects [50]. The plateau value was used as $q_{e,exp}$ for kinetic fitting; therefore, the contact-time results are discussed in terms of uptake capacity rather than removal percentage.

Adsorption isotherms

The concentration-dependent CIP data were fitted with Langmuir, Freundlich, Temkin, and Sips models. Langmuir represents monolayer adsorption on equivalent sites:

$$q_e = \frac{q_m K_L C_e}{1 + K_L C_e} \quad (14)$$

$$R_L = \frac{1}{(1 + K_L C_0)} \quad (15)$$

KL is the affinity constant; qm the fitted monolayer capacity; Ce and C0 the equilibrium and initial concentrations; and RL the separation factor. Values of $0 < RL < 1$ indicate favorable adsorption [51].

Freundlich represents adsorption on heterogeneous surfaces:

$$q_e = K_F C_e^{1/n} \quad (16)$$

KF and 1/n denote capacity and adsorption intensity, respectively; $0 < 1/n < 1$ indicates favorable adsorption [52].

Temkin assumes that adsorption heat decreases linearly with surface coverage:

$$q_e = \frac{RT}{b_T} ln(k_T C_e) \quad (17)$$

kT is the binding constant, BT = RT/bT, R the gas constant, and T the absolute temperature; BT has units of mg g−1.

Sips combines Freundlich-type behavior at low concentration with a Langmuir-type limit at high concentration:

$$q_e = \frac{q_m K_s C_e^{1/n}}{1 + K_s C_e^{1/n}} \quad (18)$$

KS, n, and qm denote affinity, heterogeneity, and fitted limiting capacity, respectively.

Sips gave the highest R^2 (0.989), followed closely by Freundlich (0.986) and Langmuir (0.978); Temkin was lower (0.931) (Fig. 5a; Table 1). The close Sips and Freundlich fits suggest surface heterogeneity but do not establish a unique adsorption mechanism.

The fitted Sips qm,fit (288.33 mg g−1) greatly exceeded the directly observed 47–48 mg g−1. The measured uptake is therefore the experimentally supported capacity; qm,fit is an extrapolated parameter requiring uncertainty and residual analysis and higher-concentration data before cross-study comparison.

Adsorption kinetics

Time-dependent CIP adsorption on $NiFe_2O_4$@CS was fitted with nonlinear pseudo-first-order (PFO), pseudo-second-order (PSO), and Elovich equations (Fig. 5b; Supplementary Table S1), used as empirical descriptors of the uptake profile under the tested conditions [53]. The PFO equation is [54]:

$$q_t = q_e(1 - e^{-1k_1 t}) \quad (19)$$

where q_e and q_t (mg g^{-1}) are the amounts adsorbed at equilibrium and time t (min), respectively, and k_1 (min^{-1}) is the PFO rate constant.

PFO gave R^2 = 0.951 and a fitted q_e of 16.25 mg g^{-1}, close to the experimental value of 16.82 mg g^{-1}, but fitted less well than PSO. The nonlinear PSO equation is:

$$q_t = \frac{t\, k_2 q_e^2}{k_2 q_e t + 1} \quad (20)$$

where k_2 (g mg^{-1} min^{-1}) is the PSO rate constant.

PSO gave the highest R^2 (0.994) and a fitted q_e of 17.59 mg g^{-1}, close to the experimental value. It therefore best described the measured data. However, PSO agreement does not prove a purely chemisorption-controlled mechanism; the reasonable PFO fit also allows contributions from physical adsorption, diffusion, and surface heterogeneity [55].

The Elovich equation for adsorption on heterogeneous surfaces is:

$$q_t = \frac{1}{\beta}\ln(\alpha\beta t + 1) \quad (21)$$

where α (mg g^{-1} min^{-1}) is the initial adsorption rate and β (g mg^{-1}) relates to desorption, surface coverage, and activation energy.

Elovich gave $R^2 = 0.825$ and was least suitable. Overall, kinetic fitting supports PSO as the best empirical model, but mechanistic interpretation must also consider the surface-charge/speciation context, FTIR changes, and DFT-supported interactions.

FTIR spectra analysis and adsorption mechanism

Fig. 6 compares the FTIR spectra of $NiFe_2O_4$@CS, CIP, and CIP-loaded $NiFe_2O_4$@CS. After adsorption, the broad 3200–3500 cm^{-1} O–H/N–H band shifted and changed intensity, supporting involvement of chitosan hydroxyl and amine groups in hydrogen bonding [56].

Changes near 1600 cm^{-1} and within 1400–1500 cm^{-1} are consistent with overlapping amide/N–H, carbonyl/carboxylate, aromatic-ring, and amine vibrations. Perturbations in the 500–800 cm^{-1} region, where ferrite metal–oxygen modes occur, also suggest possible participation of ferrite surface sites [57].

Together with the pH_{pzc} measurement and the surface-charge/speciation context at pH 7.0, these shifts support a proposed multi-interaction mechanism involving hydrogen bonding, electrostatic attraction, and possible coordination-like contacts between CIP O/N donor groups, chitosan –OH/–NH_2 groups, and ferrite metal–oxygen sites [14]. Because FTIR shifts are not uniquely diagnostic, this interpretation is evaluated alongside the DFT results.

DFT investigation

Structural optimization and stability

The optimized finite-cluster geometries of $NiFe_2O_4$, CS, CIP, $NiFe_2O_4$@CS, and $NiFe_2O_4$@CS–CIP are shown in Fig. 7. All structures converged at the CAM-B3LYP/LanL2DZ-D3(BJ) level; the RMSD values in Supplementary Table S2 indicate numerical convergence within the selected models, not validation of bulk $NiFe_2O_4$. Chitosan association rearranged metal–oxygen sites and –OH/–NH_2 groups, and CIP binding produced further local adjustment at the hybrid interface [58].

Vibrational analysis: IR and Raman spectra

Simulated IR and Raman spectra (Supplementary Fig. S2) qualitatively support the experimental FTIR interpretation. Low-frequency modes arise mainly from ferrite metal–oxygen vibrations, whereas mid-frequency modes include chitosan –NH, –OH, and C–O contributions. CIP association shifted and changed C=O, C–F, and N–H modes, consistent with hydrogen bonding and electrostatic or coordination-like interactions. Because finite models were used, the spectra are not treated as direct reproductions of the solid-state measurements.

Charge distribution and electrostatic potential

Mulliken charges (Supplementary Fig. S3) show electron-density redistribution after formation of $NiFe_2O_4$@CS and after CIP association. As these charges are basis-set dependent, they are used qualitatively. CIP O and N atoms appear as potential donor sites, consistent with the ESP maps (Supplementary Fig. S4), which locate electron-rich regions around O/N groups and electron-deficient regions near metal centers and protonated chitosan sites [59].

Noncovalent interaction (NCI) analysis

The NCI plots (Supplementary Fig. S5) show green isosurfaces between CIP and $NiFe_2O_4$@CS, indicating weak attractive dispersion/van der Waals contacts, and blue–green regions associated with stronger local attraction, including hydrogen bonding. Limited red signal in the interaction zone indicates little steric repulsion in the optimized configuration. The results therefore support multiple noncovalent contacts rather than a single binding mode [60].

Frontier molecular orbitals and electronic properties

FMO maps (Supplementary Fig. S6) show that $NiFe_2O_4$ frontier orbitals are concentrated on metal–oxygen regions and extend partly toward chitosan after composite formation. In $NiFe_2O_4$@CS–CIP, the HOMO is mainly associated with the organic components, whereas the LUMO includes ferrite contributions. The HOMO–LUMO separation decreased from 5.98 to 4.84 eV after CIP association (Supplementary Table S2), demonstrating perturbation of the finite-cluster electronic structure. These values are cluster-orbital descriptors, not experimental bulk band gaps or evidence of enhanced semiconductor performance [61].

Global chemical reactivity descriptors

Global reactivity descriptors (Supplementary Table S3) show the same trend: hardness decreased from 2.99 to 2.42 eV and softness increased from 0.334 to 0.413 eV^{-1} after CIP association, suggesting greater model polarizability. Changes in chemical potential, electronegativity, and electrophilicity further indicate altered donor–acceptor character. These descriptors compare the selected structures and are not direct thermodynamic measurements [62].

Adsorption energy and model-level binding favorability

The adsorption energy, $E_{ads} = -0.6069$ eV (Supplementary Table S2), indicates favorable CIP association within the finite-cluster model and is consistent with hydrogen-bonding, electrostatic, dispersion, and possible coordination-like contacts. Because explicit solvent, entropy, and concentration effects were not fully included, it does not establish macroscopic spontaneity or exothermicity in the aqueous batch system.

Work-function-related descriptor and surface reactivity

The work-function-related descriptor decreased from 5.65 to 4.92 eV after CIP association (Supplementary Table S2), indicating electronic-density redistribution in the optimized model. This calculated change may guide future electrochemical studies but does not demonstrate experimental CIP sensing.

Optical properties: simulated UV–visible absorption

Simulated UV–visible spectra (Supplementary Fig. S7) show red-shifted transitions after chitosan modification and CIP association, consistent with increased electronic coupling in the finite model. These shifts are computational descriptors and do not demonstrate a bulk optical band-gap reduction [63].

Structure-property-adsorption relationships

Experimental characterization supports formation of a chitosan-modified ferrite containing O- and N-bearing groups. The adsorption experiments were conducted at pH 7.0, close to the measured pH_{pzc}, where zwitterionic CIP can interact with mixed surface sites. The DFT models complement these observations by showing charge/orbital redistribution and noncovalent contacts after CIP association.

Together, the evidence supports a proposed mechanism involving hydrogen bonding, electrostatic attraction, dispersion, and possible coordination-like contacts among CIP O/N groups, chitosan –OH/–NH_2 groups, and ferrite metal–oxygen sites.

The calculations remain finite-model descriptors; claims concerning bulk band gaps, sensing, magnetic recovery, regeneration, leaching stability, or real-water performance require dedicated experiments.

Conclusion

In this work, a chitosan-modified nickel ferrite composite ($NiFe_2O_4$@CS) was prepared through a *Foeniculum vulgare* seed-extract-assisted ferrite synthesis followed by chitosan incorporation, and its CIP uptake was examined under batch conditions. XRD verified the spinel $NiFe_2O_4$ phase, while XPS, FTIR, SEM/TEM, and EDS collectively supported formation of a chitosan-modified ferrite composite containing oxygen- and nitrogen-bearing surface groups. These results support composite formation rather than proving a uniform core–shell coating. Scherrer analysis gave an apparent crystallite-size estimate of about 16.5 nm after composite formation; this value should be interpreted as an XRD peak-broadening-derived estimate rather than direct evidence of physical particle shrinkage. The measured pH_{pzc} of the composite was 6.97, and adsorption measurements were conducted at pH 7.0. The contact-time experiment approached an experimental uptake of 16.82 mg g^{-1} under the kinetic-test conditions, whereas the six-point concentration-dependent 120-min endpoint experiment reached a highest directly

measured uptake of about 47–48 mg g^{-1} within the tested range. The kinetic data were best represented by the pseudo-second-order equation, indicating that surface-site availability and interaction processes strongly influenced the uptake profile, although this empirical model alone does not prove a unique chemisorption mechanism. Isotherm fitting gave the highest R^2 value for the Sips model, suggesting that this heterogeneous-site equation described the endpoint data better than the tested alternatives. However, the fitted Sips $q_{m,fit}$ value should be treated as a model-derived extrapolated parameter, not as a directly measured maximum adsorption capacity. FTIR shifts and DFT calculations supported a multi-interaction adsorption mechanism involving hydrogen bonding, electrostatic contributions, and possible coordination-like contacts among CIP functional groups, chitosan –OH/–NH_2 groups, and ferrite metal–oxygen sites. The DFT adsorption energy of −0.6069 eV indicates favorable binding for the selected finite-cluster model, but it should not be interpreted as complete thermodynamic proof of experimental spontaneity or exothermicity. Overall, $NiFe_2O_4$@CS is a promising ferrite-biopolymer adsorbent candidate for CIP removal under the tested single-solute batch conditions. Further work should include uncertainty quantification and model confidence intervals, parent-material controls using CS, $NiFe_2O_4$, and physical mixtures, as well as regeneration, magnetic recovery, leaching/stability, and real or simulated wastewater tests before practical application claims are made.

Data availability

The datasets generated and/or analyzed during the current study are available from the corresponding author on reasonable request.

References

1. aus der Beek, T. et al. Pharmaceuticals in the environment: Global occurrences and perspectives. Environ. Toxicol. *Chem.* **35,** 823–835 (2016). https://doi.org/10.1002/etc.3339

2. Wilkinson, J. L. et al. Pharmaceutical pollution of the world's rivers. Proc. Natl. Acad. Sci. *U.S.A.* **119,** e2113947119 (2022). https://doi.org/10.1073/pnas.2113947119

3. Bengtsson-Palme, J. & Larsson, D. G. J. Concentrations of antibiotics predicted to select for resistant bacteria: Proposed limits for environmental regulation. Environ. *Int.* **86,** 140–149 (2016). https://doi.org/10.1016/j.envint.2015.10.015

4. Larsson, D. G. J. & Flach, C.-F. Antibiotic resistance in the environment. Nat. Rev. *Microbiol.* **20,** 257–269 (2022). https://doi.org/10.1038/s41579-021-00649-x

5. Younis, A., Alfaiz, M., Alrasheedi, M. & Almotiry, S. Removal of pharmaceutical pollutants from aquatic mediums using MXene nanocomposites: Mechanisms, advances, and challenges. Egypt. J. Aquat. Biol. *Fish.* **29,** 1231–1261 (2025). https://doi.org/10.21608/ejabf.2025.431759.6766

6. Florindo, C., Lima, F., Branco, L. C. & Marrucho, I. M. Hydrophobic deep eutectic solvents: A circular approach to purify water contaminated with ciprofloxacin. ACS Sustain. Chem. *Eng.* **7,** 14739–14746 (2019). https://doi.org/10.1021/acssuschemeng.9b02658

7. Siddiquee, A. et al. Binding study of antibacterial drug ciprofloxacin with imidazolium-based ionic liquids having different halide anions: A spectroscopic and density functional theory analysis. *ACS Omega* **8,** 42699–42710 (2023). https://doi.org/10.1021/acsomega.3c05100

8. Alqarni, L. S., Alharbi, A. A., Ben Aissa, M. A. & Modwi, A. Fabrication of green ternary CeO_2@Co_3O_4@g-C_3N_4 nanocomposite as an efficient and durable sorbent for ciprofloxacin removal. J. Indian Chem. *Soc.* **102,** 102129 (2025). https://doi.org/10.1016/j.jics.2025.102129

9. Tripathy, S. P. et al. Mixed-valence bimetallic Ce/Zr MOF-based nanoarchitecture: A visible-light-active photocatalyst for ciprofloxacin degradation and hydrogen evolution. *Langmuir* **38,** 1766–1780 (2022). https://doi.org/10.1021/acs.langmuir.1c02873

10. Alqarni, L. S. et al. Selective adsorption of lead (Pb^{2+}) ions from contaminated water via Y_2O_3-modified chitosan adsorbent. J. Polym. *Environ.* **34,** 30 (2026). https://doi.org/10.1007/s10924-025-03742-x

11. Younis, A. M., Aly-Eldeen, M. A. & Elkady, E. M. Effect of different molecular weights of chitosan on the removal efficiencies of heavy metals from contaminated water. Egypt. J. Aquat. Biol. *Fish.* **23,** 149–158 (2019). https://doi.org/10.21608/ejabf.2019.52591

12. Duvedi, R. K., Kumar, S., Sharma, S. K. & Batish, A. Investigating bio-inspired chitosan modification in 2D-printed PVDF/$BaTiO_3$-reduced graphene oxide matrices for advanced nanogenerators. Ceram. *Int.* **52,** 3596–3607 (2026). https://doi.org/10.1016/j.ceramint.2025.12.151

13. Gopal, G., Nirmala, M. J. & Mukherjee, A. A novel chitosan-coated Fe–Cu CNS loaded with CMC–alginate composite for adsorptive removal of ciprofloxacin from water. Surf. *Interfaces* **39,** 102981 (2023). https://doi.org/10.1016/j.surfin.2023.102981

14. Mohammed, N. A. H., Shamma, R. N., Elagroudy, S. & Adewuyi, A. Chitosan-incorporated nickel ferrite photocatalyst for complete photocatalytic degradation of ciprofloxacin, ampicillin and erythromycin in water. *Results Chem.* **7,** 101307 (2024). https://doi.org/10.1016/j.rechem.2024.101307

15. Vamsi, E. B., Reshma, M. & Devatha, C. Adsorption of ciprofloxacin antibiotic using chitosan graphene oxide hybrid beads. Case Stud. Chem. Environ. *Eng.* **10,** 100982 (2024). https://doi.org/10.1016/j.cscee.2024.100982

16. Abd El-Monaem, E. M. et al. Sustainable adsorptive removal of antibiotic residues by chitosan composites: An insight into current developments and future recommendations. Arab. J. *Chem.* **15,** 103743 (2022). https://doi.org/10.1016/j.arabjc.2022.103743

17. Shagdarova, B., Zhuikova, Y. & Il'ina, A. Adsorbent materials based on modified chitosan for purification of aqueous media from pharmaceutical residues, primarily antibiotics. *Polymers* **17,** 2601 (2025). https://doi.org/10.3390/polym17192601

18. Azzam, A. B., Tokhy, Y. A., Dars, F. M. E. & Younes, A. A. Heterogeneous porous biochar-supported nano $NiFe_2O_4$ for efficient removal of hazardous antibiotic from pharmaceutical wastewater. Environ. Sci. Pollut. *Res.* **30,** 119473–119490 (2023). https://doi.org/10.1007/s11356-023-30587-5

19. Liang, H., Zhu, C., Wang, A. & Chen, F. Facile preparation of $NiFe_2O_4$/biochar composite adsorbent for efficient adsorption removal of antibiotics in water. *Carbon Res.* **3,** 2 (2024). https://doi.org/10.1007/s44246-023-00094-w

20. Malakootian, M., Nasiri, A. & Mahdizadeh, H. Preparation of $CoFe_2O_4$/activated carbon@chitosan as a new magnetic nanobiocomposite for adsorption of ciprofloxacin in aqueous solutions. Water Sci. *Technol.* **78,** 2158–2170 (2018). https://doi.org/10.2166/wst.2018.494

21. Sharma, M. et al. Process analysis of aqueous ciprofloxacin adsorption by biochar-magnetite nanocomposites. Discov. Appl. *Sci.* **7,** 1216 (2025). https://doi.org/10.1007/s42452-025-07785-6

22. Shrivastava, A. & Sinha, I. Simultaneous adsorption of organic pollutants on Mo-doped $NiFe_2O_4$ nanoparticles: Experimental and computational studies. J. Mol. *Liq.* **430,** 127827 (2025). https://doi.org/10.1016/j.molliq.2025.127827

23. Sistanizadeh Aghdam, M., Cheraghi, M., Sobhanardakani, S., Mohammadi, A. A. & Lorestani, B. Facile fabrication of novel magnetic chitosan@Ag-MWCN nanocomposite for the adsorptive removal of ciprofloxacin from aqueous solutions. Sci. *Rep.* **15,** 5112 (2025). https://doi.org/10.1038/s41598-025-89322-4

24. Elamin, N. Y., El-Fattah, W. A. & Modwi, A. Green $NiFe_2O_4$ nano-sorbent construction via *Foeniculum vulgare* extract for efficient barium ions removal. Z. Naturforsch. *A* **78,** 851–862 (2023). https://doi.org/10.1515/zna-2023-0094

25. Kausar, A. et al. Cellulose–chitosan composites for ciprofloxacin removal from pharmaceutical wastewater: Experimental and DFT insights. *Results Chem.* **20,** 102971 (2026). https://doi.org/10.1016/j.rechem.2025.102971

26. Frisch, M. J. et al. Gaussian 16, Revision C.01. (Gaussian, Inc., Wallingford, CT, 2016).

27. Grimme, S., Antony, J., Ehrlich, S. & Krieg, H. A consistent and accurate ab initio parametrization of density functional dispersion correction (DFT-D) for the 94 elements H–Pu. J. Chem. *Phys.* **132,** 154104 (2010). https://doi.org/10.1063/1.3382344

28. Grimme, S., Ehrlich, S. & Goerigk, L. Effect of the damping function in dispersion-corrected density functional theory. J. Comput. *Chem.* **32,** 1456–1465 (2011). https://doi.org/10.1002/jcc.21759

29. Hay, P. J. & Wadt, W. R. Ab initio effective core potentials for molecular calculations. Potentials for the transition metal atoms Sc to Hg. J. Chem. *Phys.* **82,** 270–283 (1985). https://doi.org/10.1063/1.448799

30. Yanai, T., Tew, D. P. & Handy, N. C. A new hybrid exchange-correlation functional using the Coulomb-attenuating method (CAM-B3LYP). Chem. Phys. *Lett.* **393,** 51–57 (2004). https://doi.org/10.1016/j.cplett.2004.06.011

31. Parr, R. G., von Szentpály, L. & Liu, S. Electrophilicity index. J. Am. Chem. *Soc.* **121,** 1922–1924 (1999). https://doi.org/10.1021/ja983494x

32. Zhan, C.-G., Nichols, J. A. & Dixon, D. A. Ionization potential, electron affinity, electronegativity, hardness, and electron excitation energy: Molecular properties from density functional theory orbital energies. J. Phys. Chem. *A* **107,** 4184–4195 (2003). https://doi.org/10.1021/jp0225774

33. Abdel-Raouf, M. E.-S. et al. Chitosan-based architectures as an effective approach for the removal of some toxic species from aqueous media. *ACS Omega* **8,** 10086–10099 (2023). https://doi.org/10.1021/acsomega.2c07264

34. Alves, F. F. C. et al. A new composite based on gellan gum/chitosan and hydroxyapatite contains gallium for removing the anionic dyes Remazol Blue and Remazol Red. J. Polym. *Environ.* **32,** 560–572 (2024). https://doi.org/10.1007/s10924-023-02993-w

35. Upadhyay, A., Alimohammadi, F. & Tehrani, R. Engineering porosity-tuned chitosan beads: Balancing porosity, kinetics, and mechanical integrity. *ACS Omega* **9,** 33857–33867 (2024). https://doi.org/10.1021/acsomega.4c03583

36. Hariharasuthan, R., Chitradevi, S., Radha, K. & Chithambaram, V. Characterization of $NiFe_2O_4$ (nickel ferrite) nanoparticles with very low magnetic saturation synthesized via co-precipitation method. Appl. Phys. *A* **128,** 1045 (2022). https://doi.org/10.1007/s00339-022-06163-y

37. Kesavan, G., Nataraj, N., Chen, S.-M. & Lin, L.-H. Hydrothermal synthesis of $NiFe_2O_4$ nanoparticles as an efficient electrocatalyst for the electrochemical detection of bisphenol A. New J. *Chem.* **44,** 7698–7707 (2020). https://doi.org/10.1039/D0NJ00608D

38. Xu, X., Li, Y., Zhang, G., Yang, F. & He, P. NiO-$NiFe_2O_4$-rGO magnetic nanomaterials for activated peroxymonosulfate degradation of Rhodamine B. *Water* **11,** 384 (2019). https://doi.org/10.3390/w11020384

39. El Bendali, A. et al. The electrochemical and structural changes of phosphorus-doped TiO_2 through in situ Raman and in situ X-ray diffraction analysis. *ACS Omega* **9,** 14911–14922 (2024). https://doi.org/10.1021/acsomega.3c08122

40. Gabal, M., Kosa, S. & Almutairi, T. Cr-substitution effect on the structural and magnetic properties of nano-sized $NiFe_2O_4$ prepared via novel chitosan route. J. Magn. Magn. *Mater.* **356,** 37–41 (2014). https://doi.org/10.1016/j.jmmm.2013.12.044

41. Al-Farraj, E. S. et al. Fabrication of hybrid nanocomposite derived from chitosan as efficient electrode materials for supercapacitor. Int. J. Biol. *Macromol.* **120,** 2271–2278 (2018). https://doi.org/10.1016/j.ijbiomac.2018.08.104

42. Homayonfard, A., Miralinaghi, M., Haji Seyed Mohammad Shirazi, R. & Moniri, E. Removal of Cd(II) ion from aqueous solution using nickel ferrite magnetic nanoparticles cross-linked chitosan. J. *Water Wastewater* **31,** 112–127 (2020). https://doi.org/10.22093/wwj.2019.118849.2631

43. Thakurata, D. G., Paul, A., Das, K. C. & Dhar, S. S. Fabrication of hierarchical bentonite/chitosan/$NiFe_2O_4$ ternary nanocomposite and its efficiency in the removal of Pb(II) from aqueous medium. Environ. Eng. *Res.* **26,** 200216 (2021). https://doi.org/10.4491/eer.2020.216

44. Yue, X., Zhao, J., Shi, H., Chi, Y. & Salam, M. Preparation of composite adsorbents of activated carbon-supported MgO/MnO_2 and adsorption of Rhodamine B. Water Sci. *Technol.* **81,** 906–914 (2020). https://doi.org/10.2166/wst.2020.172

45. Wang, C.-J., Li, Z., Jiang, W.-T., Jean, J.-S. & Liu, C.-C. Cation exchange interaction between antibiotic ciprofloxacin and montmorillonite. J. Hazard. *Mater.* **183,** 309–314 (2010). https://doi.org/10.1016/j.jhazmat.2010.07.025

46. Chueachot, R. et al. Adsorption efficiency of methylene blue from aqueous solution with amine-functionalized mesoporous silica nanospheres by co-condensation biphasic synthesis: Adsorption condition and equilibrium studies. *Mater. Today Proc.* **5,** 14079–14085 (2018). https://doi.org/10.1016/j.matpr.2018.02.066

47. Czyrski, A. The spectrophotometric determination of lipophilicity and dissociation constants of ciprofloxacin and levofloxacin. *Spectrochim. Acta A Mol. Biomol. Spectrosc.* **265,** 120343 (2022). https://doi.org/10.1016/j.saa.2021.120343

48. Gu, C. & Karthikeyan, K. Sorption of the antimicrobial ciprofloxacin to aluminum and iron hydrous oxides. *Environ. Sci. Technol.* **39,** 9166–9173 (2005). https://doi.org/10.1021/es051109f

49. MacKay, A. A. & Seremet, D. E. Probe compounds to quantify cation exchange and complexation interactions of ciprofloxacin with soils. *Environ. Sci. Technol.* **42,** 8270–8276 (2008). https://doi.org/10.1021/es800984x

50. Sircar, S. Adsorbate mass transfer into porous adsorbents—A practical viewpoint. Sep. Purif. *Technol.* **192,** 383–400 (2018). https://doi.org/10.1016/j.seppur.2017.10.014

51. Danalıoğlu, S. T., Kerkez Kuyumcu, Ö., Abdel Salam, M. & Bayazit, Ş. S. Chitosan-grafted SiO_2–Fe_3O_4 nanoparticles for removal of antibiotics from water. Environ. Sci. Pollut. *Res.* **25,** 36661–36670 (2018). https://doi.org/10.1007/s11356-018-3573-y

52. Balarak, D., Mahvi, A. H., Shim, M. J. & Lee, S.-M. Adsorption of ciprofloxacin from aqueous solution onto synthesized NiO: Isotherm, kinetic and thermodynamic studies. Desalin. *Water Treat.* **212,** 390–400 (2021). https://doi.org/10.5004/dwt.2021.26603

53. Reynaud, F. et al. Spray-dried chitosan-metal microparticles for ciprofloxacin adsorption: Kinetic and equilibrium studies. *Soft Matter* **7,** 7304–7312 (2011). https://doi.org/10.1039/C1SM05509G

54. Avcı, A., İnci, İ. & Baylan, N. A comparative adsorption study with various adsorbents for the removal of ciprofloxacin hydrochloride from water. *Water Air Soil Pollut.* **230,** 250 (2019). https://doi.org/10.1007/s11270-019-4315-6

55. Levy, J., Berhane, T., Krekeler, M. P. & Danielson, N. Kinetic sorption of contaminants of emerging concern by a palygorskite-montmorillonite filter medium. *Geol. Soc. Am. Abstr. Programs*, 285984 (2016). https://doi.org/10.1130/abs/2016am-285984

56. Mabrouk, M., Abd El-Wahab, R. M., Beherei, H. H., Selim, M. M. & Das, D. B. Multifunctional magnetite nanoparticles for drug delivery: Preparation, characterisation, antibacterial properties and drug release kinetics. Int. J. *Pharm.* **587,** 119658 (2020). https://doi.org/10.1016/j.ijpharm.2020.119658

57. Gor, A. H. & Dave, P. N. Adsorptive abatement of ciprofloxacin using $NiFe_2O_4$ nanoparticles incorporated into G. ghatti-cl-P(AAm) nanocomposites hydrogel: Isotherm, kinetic, and thermodynamic studies. Polym. *Bull.* **77,** 5589–5613 (2020). https://doi.org/10.1007/s00289-019-03032-2

58. Mustafa, G. et al. Synthesis of polymeric ferrite composites (Ni-$CoFe_2O_4$/chitosan, Zn-$NiFe_2O_4$/starch, Co-$NiZnFe_2O_4$/polyaniline, Ni-doped $CrZnFe_2O_4$/alginate, and Cr-doped $ZnCoFe_2O_4$/PVA) for the removal of reactive golden yellow-160 dye from wastewater. J. Environ. Chem. *Eng.* **12,** 112581 (2024). https://doi.org/10.1016/j.jece.2024.112581

59. Şenol, Z. M., Ertap, H., Fernine, Y. & El Messaoudi, N. Adsorptive removal of synthetic dye from its aqueous solution by using chitosan-bentonite composite: DFT and experimental studies. Polym. *Bull.* **81,** 12795–12817 (2024). https://doi.org/10.1007/s00289-024-05323-9

60. Johnson, E. R. et al. Revealing noncovalent interactions. J. Am. Chem. *Soc.* **132,** 6498–6506 (2010). https://doi.org/10.1021/ja100936w

61. Kumar, P. V., Short, M. P., Yip, S., Yildiz, B. & Grossman, J. C. High surface reactivity and water adsorption on $NiFe_2O_4$(111) surfaces. J. Phys. Chem. *C* **117,** 5678–5683 (2013). https://doi.org/10.1021/jp309434a

62. Latif, M. et al. Evaluation of tetracycline photocatalytic degradation using $NiFe_2O_4/CeO_2$/GO nanocomposite for environmental remediation: In silico molecular docking, antibacterial performance, degradation pathways, and DFT calculations. Sep. Purif. *Technol.* **351,** 128074 (2024). https://doi.org/10.1016/j.seppur.2024.128074

63. Khalaji, A. D. $NiFe_2O_4$ prepared by the chitosan-assisted route for the photodegradation of methylene blue under simulated sunlight irradiation. Chem. Phys. *Impact* **8,** 100652 (2024). https://doi.org/10.1016/j.chphi.2024.100652

Acknowledgements

The Researchers would like to thank the Deanship of Graduate Studies and Scientific Research at Qassim University (www.qu.edu.sa) for financial support (QU-APC-2026).

Funding

This research did not receive any specific grant from funding agencies in the public, commercial or not-for-profit sectors.

Author contributions

A.M.Y.: Conceptualization, methodology, investigation, data curation, formal analysis, and writing—original draft. M.A.B.A.: Methodology, formal analysis, visualization, and writing—review and editing. S.A.: Investigation, validation, and writing—review and editing. R.B.S.: Investigation, validation, and writing—review and editing. A.B.A.: Software, formal analysis, visualization, and writing—review and editing. A.M.: Conceptualization, supervision, project administration, resources, validation, and writing—review and editing. A.A.: Software, formal analysis, visualization, and writing—review and editing. All authors reviewed and approved the final manuscript.

Additional information

Competing interests

The authors declare no competing interests.

Figure legends

Figure 1. X-ray diffraction patterns of the constituent materials and nanocomposite. Patterns are shown for chitosan (CS), $NiFe_2O_4$, and $NiFe_2O_4$@CS.

Figure 2. X-ray photoelectron spectra of $NiFe_2O_4$@CS. (a) Survey spectrum and high-resolution spectra of (b) Ni 2p, (c) Fe 2p, (d) O 1s, (e) C 1s, and (f) N 1s.

Figure 3. Electron microscopy of $NiFe_2O_4$@CS. (a–c) Scanning electron micrographs and (d) a transmission electron micrograph with representative particle/domain measurements.

Figure 4. Batch adsorption measurements for $NiFe_2O_4$@CS. (a) Concentration-dependent 120-min endpoint uptake, (b) pH-drift determination of the point of zero charge, and (c) the contact-time uptake profile. Symbols show mean values from three replicate experiments (n = 3).

Figure 5. Nonlinear isotherm and kinetic fits for CIP adsorption by $NiFe_2O_4$@CS. (a) Isotherm models fitted to the 120-min concentration-dependent endpoint data and (b) kinetic models fitted to the contact-time data. Symbols show mean values from three replicate experiments (n = 3).

Figure 6. FTIR spectra before and after CIP adsorption. Spectra are shown for $NiFe_2O_4$@CS, ciprofloxacin (CIP), and CIP-loaded $NiFe_2O_4$@CS.

Figure 7. Optimized finite-cluster geometries used in the DFT calculations. Structures are shown for $NiFe_2O_4$, CS, CIP, $NiFe_2O_4$@CS, and $NiFe_2O_4$@CS–CIP.

Tables

Table 1. Nonlinear isotherm-model parameters for the 120-min concentration-dependent CIP adsorption data.

Equilibrium model	Parameter	Value
Langmuir	q_m (mg g^{-1})	72.16
Langmuir	K_L (L mg^{-1})	0.02
Langmuir	R^2	0.978
Freundlich	$1/n$	0.57
Freundlich	K_F [mg g^{-1} (L $mg^{-1})^{1/n}$]	3.92
Freundlich	R^2	0.986
Temkin	B_T (mg g^{-1})	10.21
Temkin	K_T (L mg^{-1})	0.72
Temkin	R^2	0.931
Sips	$q_{m,fit}$ (mg g^{-1})	288.33
Sips	K_S (L mg^{-1})	9.61
Sips	n	0.63
Sips	R^2	0.989

Note: The fitted Sips $q_{m,fit}$ is an extrapolated model parameter and should not be treated as a directly measured maximum capacity without uncertainty and residual analyses.

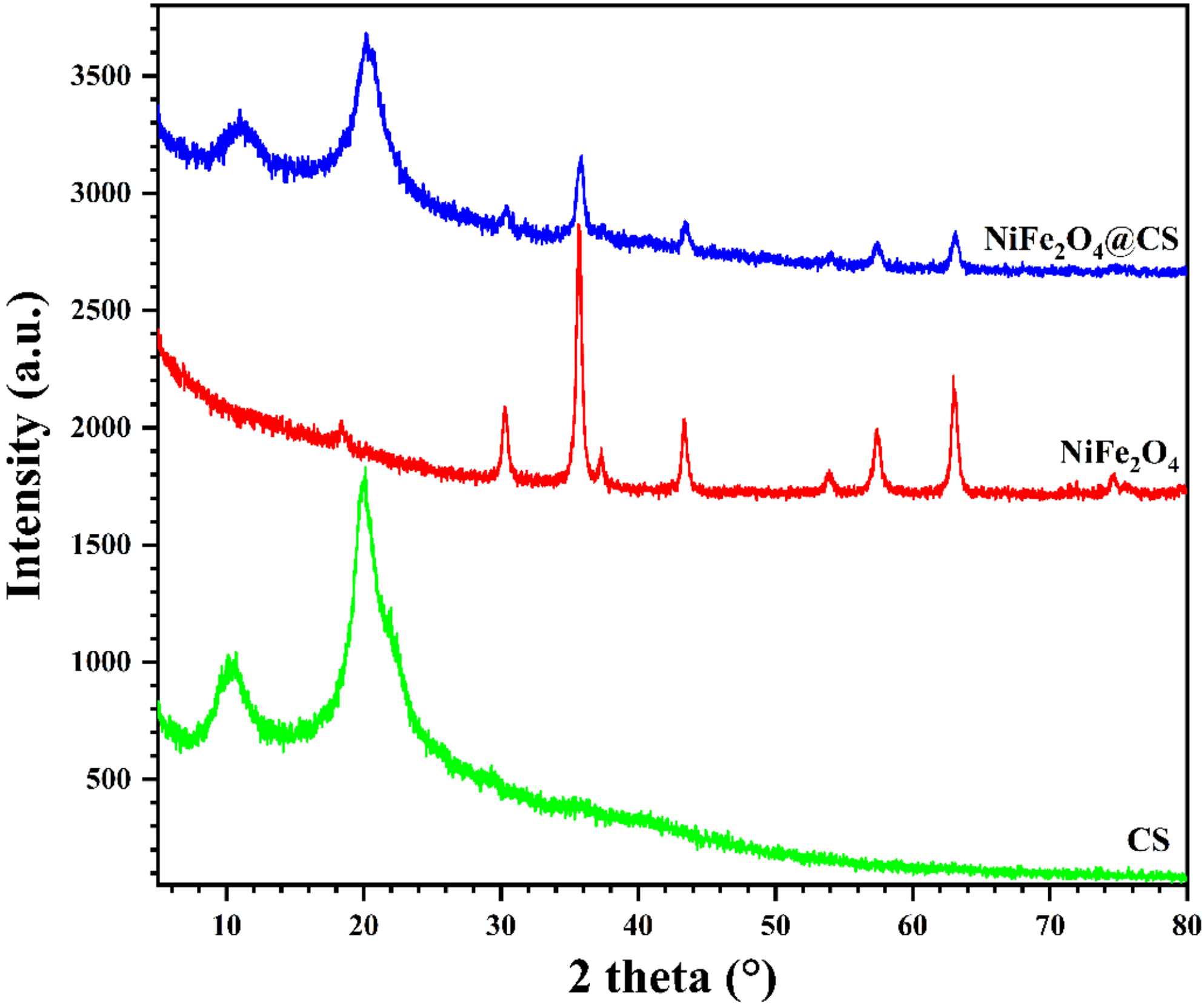
Intensity (a.u.)
3500
3000
2500
2000
1500
1000
500
10
20
30
40
50
60
70
80
2 theta (°)
NiFe2O4@CS
NiFe2O4
CS

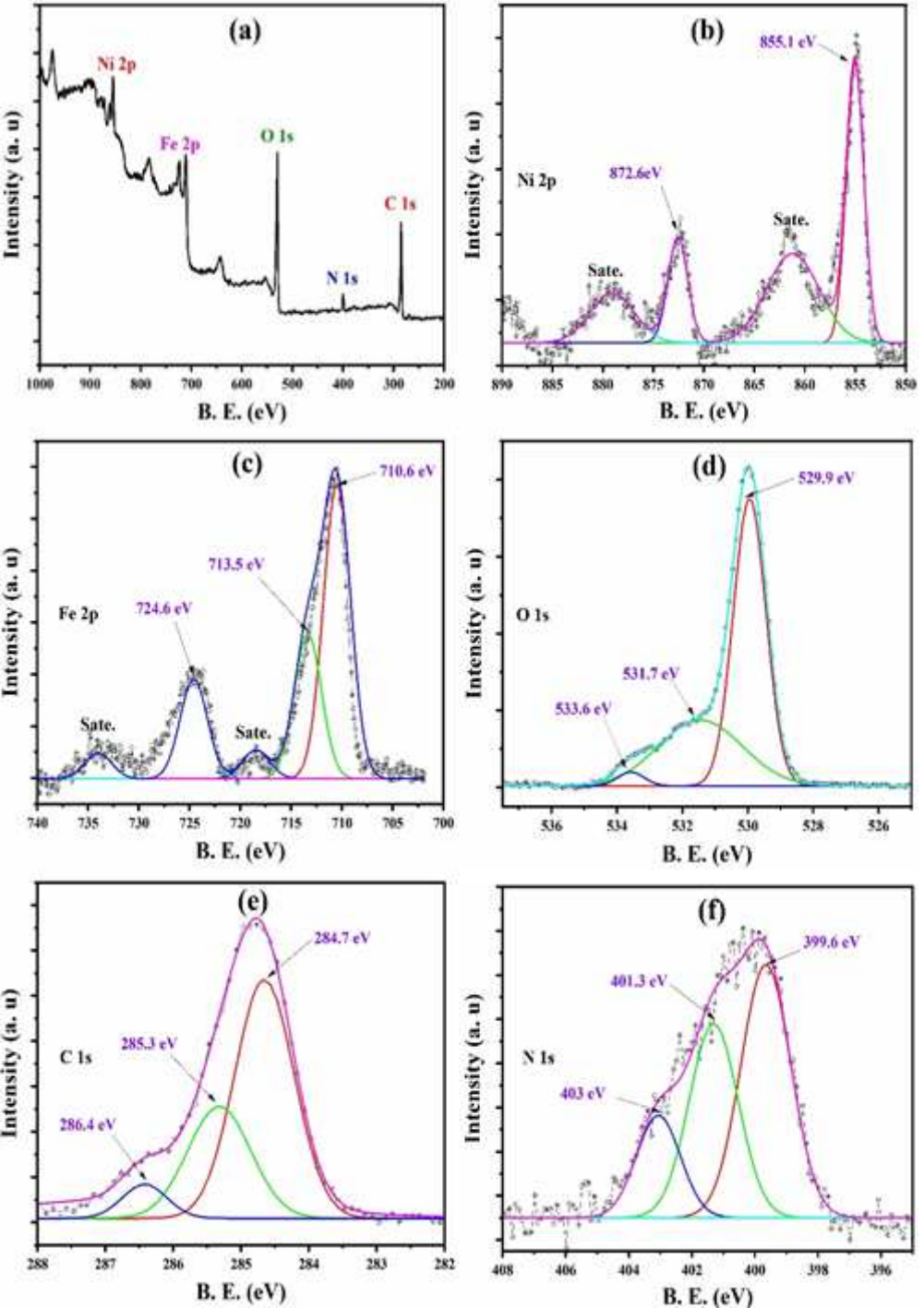
(a)
Ni 2p
Fe 2p
O 1s
C 1s
N 1s
Intensity (a. u)
B. E. (eV)
(b)
855.1 eV
872.6eV
Ni 2p
Sate.
Sate.
Intensity (a. u)
B. E. (eV)
(c)
710.6 eV
713.5 eV
724.6 eV
Fe 2p
Sate.
Sate.
Intensity (a. u)
B. E. (eV)
(d)
529.9 eV
O 1s
531.7 eV
533.6 eV
Intensity (a. u)
B. E. (eV)
(e)
284.7 eV
285.3 eV
C 1s
286.4 eV
Intensity (a. u)
B. E. (eV)
(f)
399.6 eV
401.3 eV
N 1s
403 eV
Intensity (a. u)
B. E. (eV)

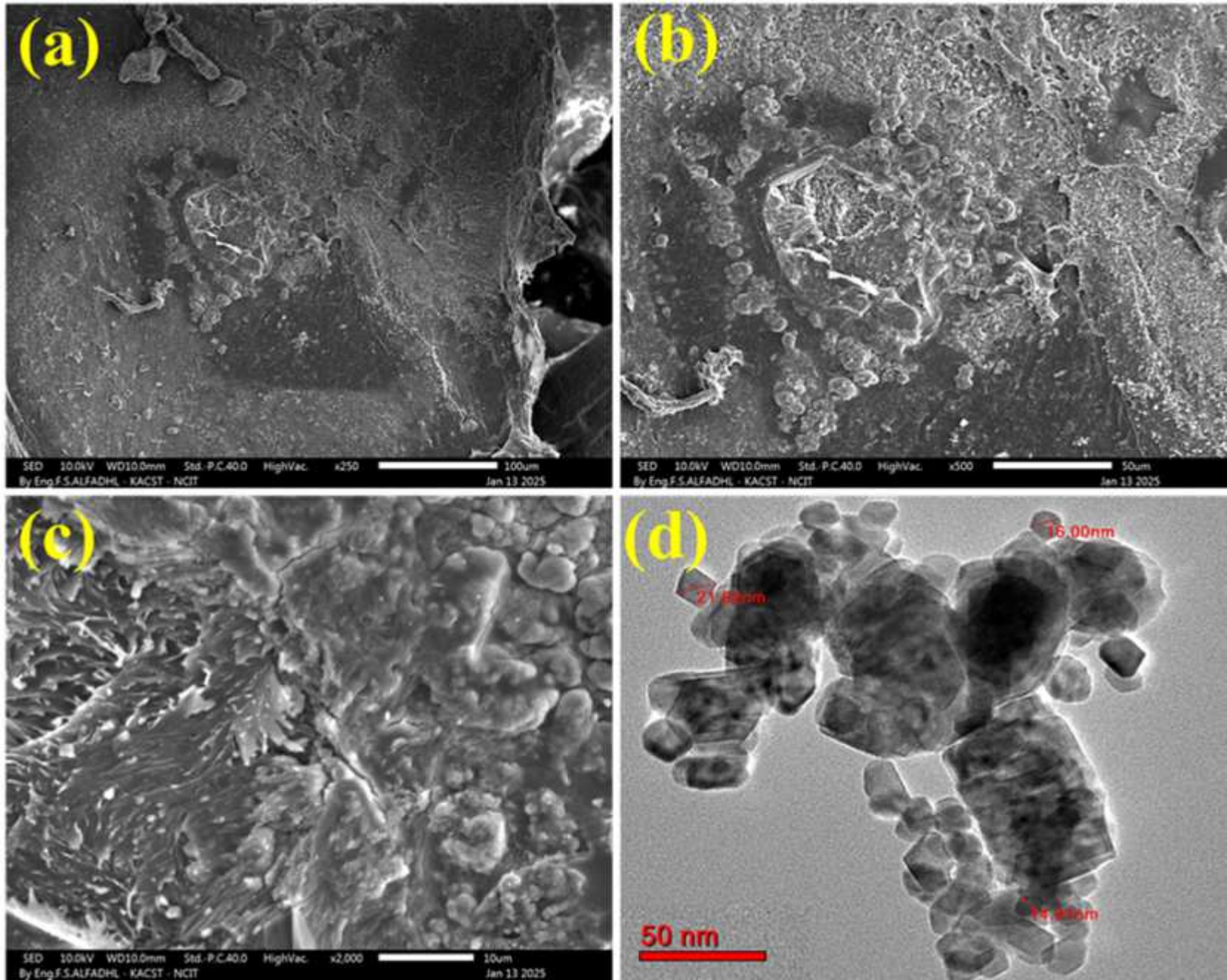
(a)
SED 10.0kV WD10.0mm Std. P.C.40.0 HighVac. x250 100um
By Eng.F.S.ALFADHL - KACST - NCIT Jan 13 2025
(b)
SED 10.0kV WD10.0mm Std. P.C.40.0 HighVac. x500 50um
By Eng.F.S.ALFADHL - KACST - NCIT Jan 13 2025
(c)
SED 10.0kV WD10.0mm Std. P.C.40.0 HighVac. x2,000 10um
By Eng.F.S.ALFADHL - KACST - NCIT Jan 13 2025
(d)
16.00nm
50 nm

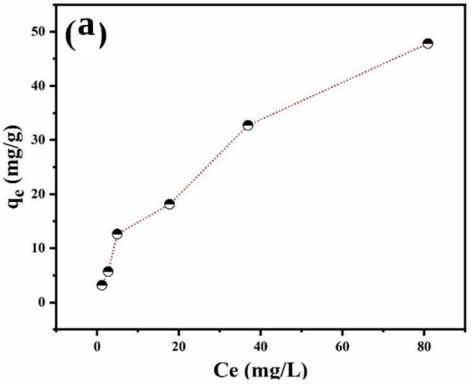
(a)
q_e (mg/g)
Ce (mg/L)

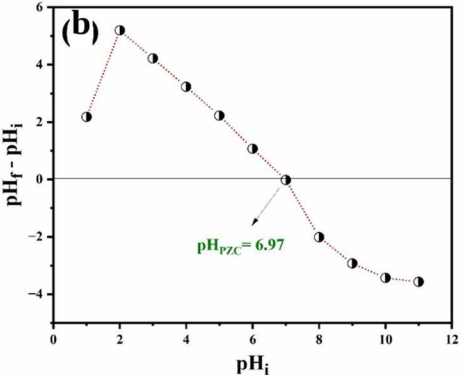
(b)
$pH_f - pH_i$
pH_i
pH_{PZC}= 6.97

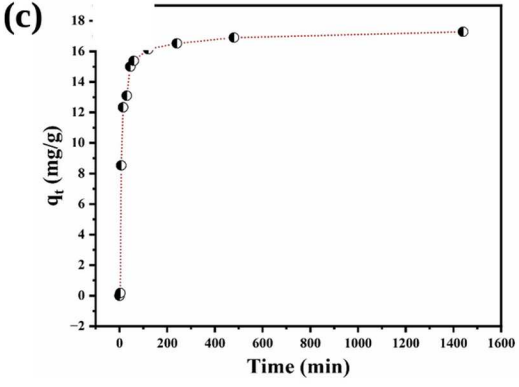
(c)
q_t (mg/g)
Time (min)

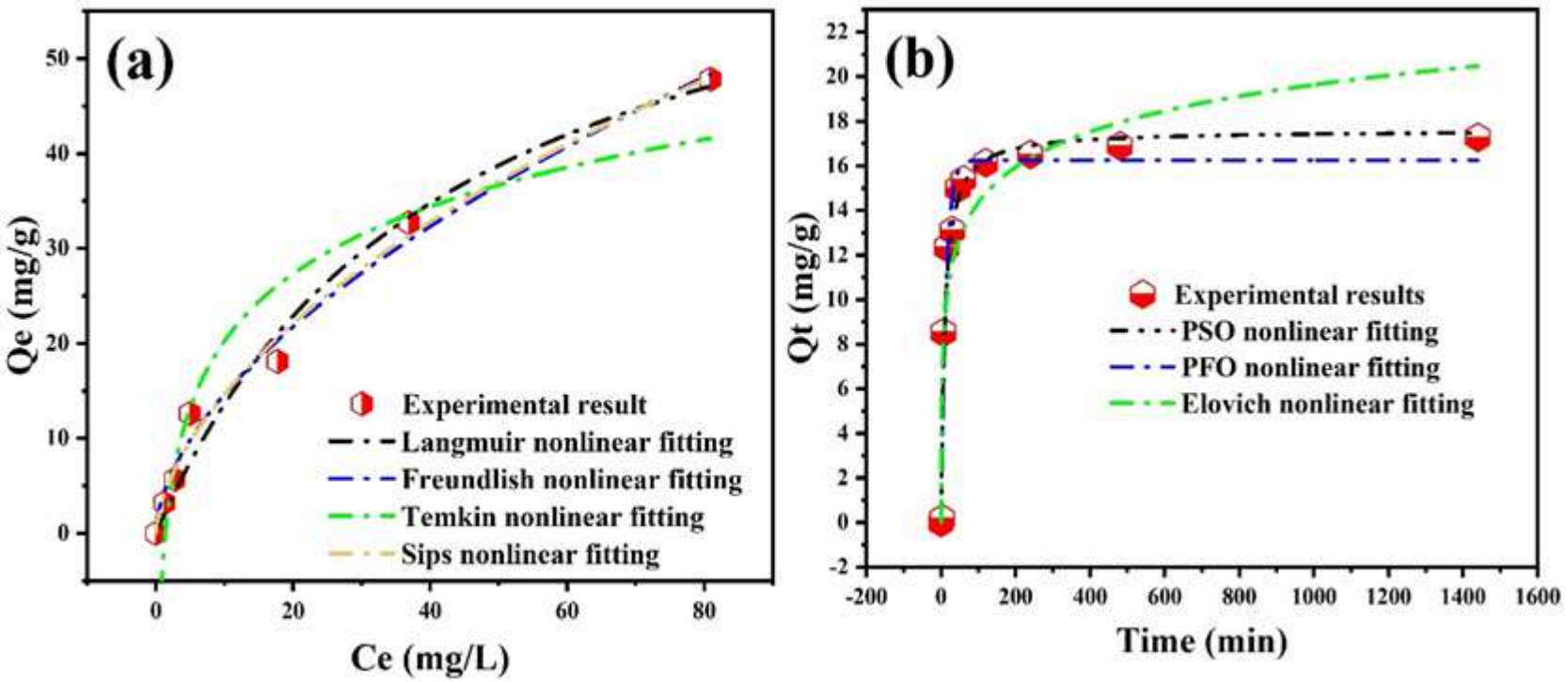
(a)
Qe (mg/g)
Ce (mg/L)
Experimental result
Langmuir nonlinear fitting
Freundlish nonlinear fitting
Temkin nonlinear fitting
Sips nonlinear fitting
(b)
Qt (mg/g)
Time (min)
Experimental results
PSO nonlinear fitting
PFO nonlinear fitting
Elovich nonlinear fitting

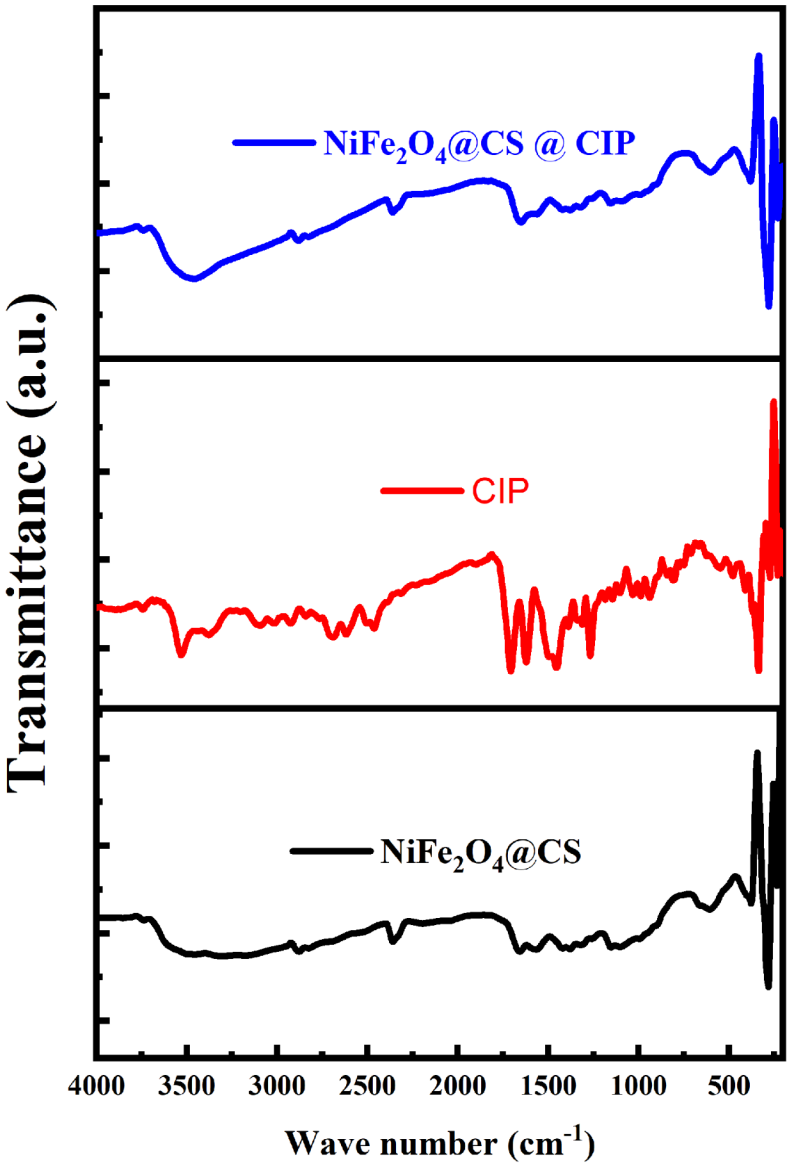
NiFe2O4@CS @ CIP
CIP
NiFe2O4@CS
Transmittance (a.u.)
4000
3500
3000
2500
2000
1500
1000
500
Wave number (cm-1)

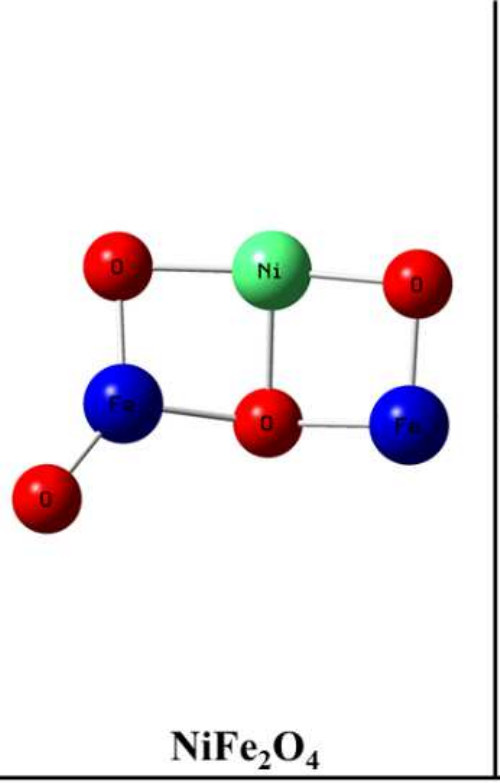

$NiFe_2O_4$

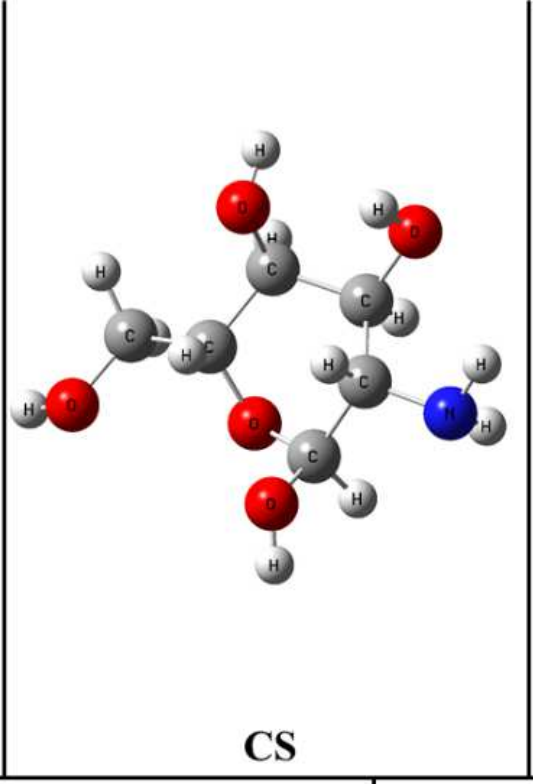

CS

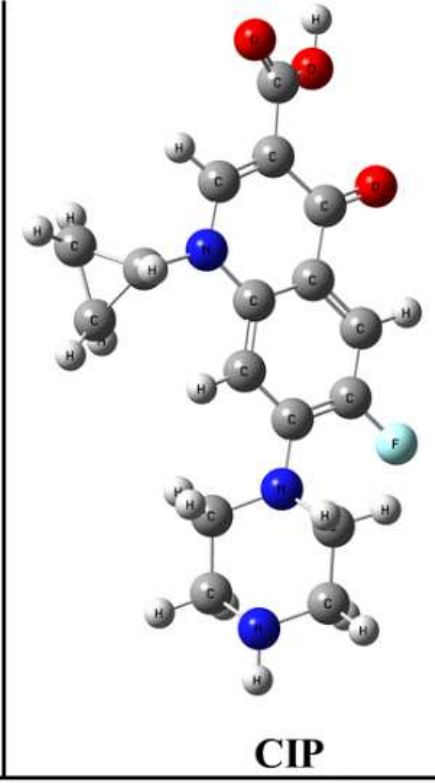

CIP

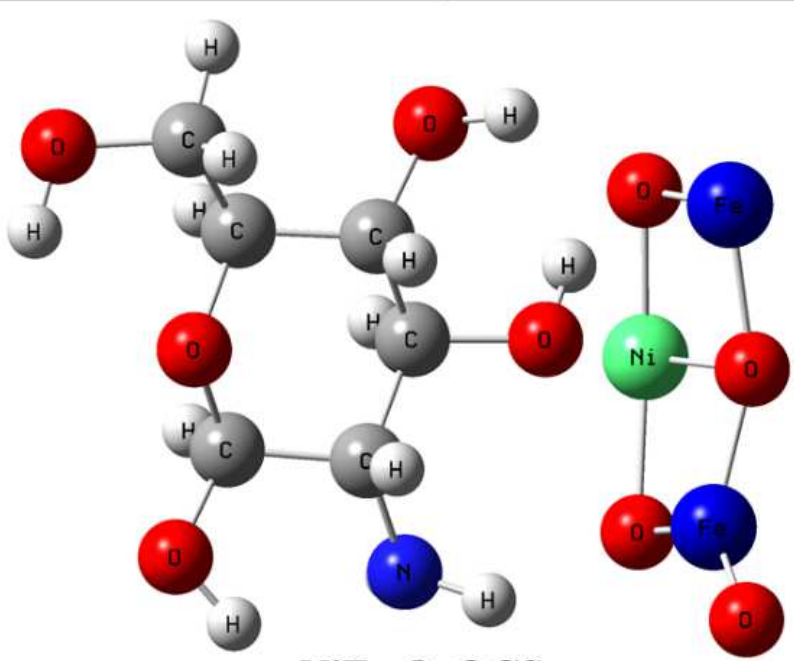

$NiFe_2O_4$@CS

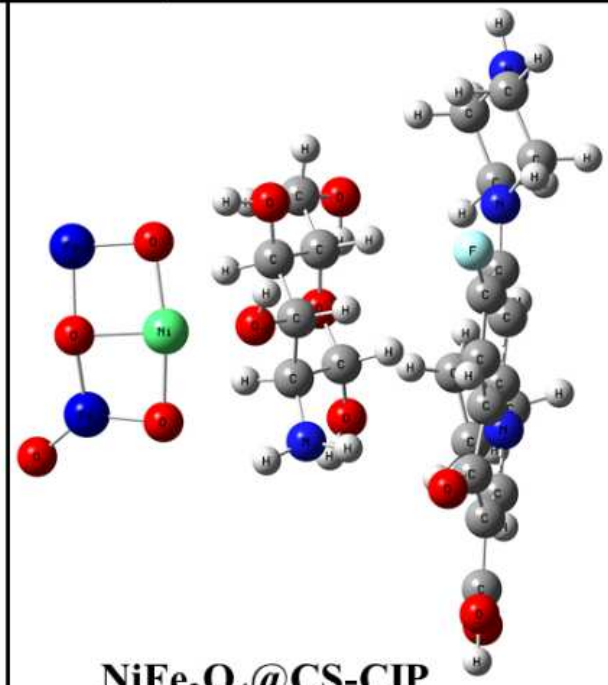

$NiFe_2O_4$@CS-CIP

Supplementary Files

This is a list of supplementary files associated with this preprint. Click to download.

- 02SupplementaryInformationScientificReports.pdf